Refinement and Spheroidization of Primary Silicon Particles in Eutectic-Divorced Hypereutectic Al–Si Alloy and Their Impact on Wear Resistance

YUNA WU, CHENGCHENG HAN, ZONGHAN LI, YITONG HU, CHEN CHEN, JINGHUA JIANG, HENGCHENG LIAO, and YONGHAO ZHAO

Hypereutectic Al–Si alloys are limited in industrial applications because they contain coarse and angular primary silicon particles (PSPs). In this study, we employ a novel casting process, glass tube suction casting (GTSC), combined with solid-solution treatment to refine and spheroidize PSPs in a eutectic-divorced hypereutectic Al–Si alloy (A390) and increase its wear resistance. Following solid-solution treatment at 520 °C for 4 hours, the average equivalent diameter (*D*) of the PSPs decreases from 18.8 to 5.2 μm, and the wear loss rate of mass decreases from 55.5 to 14.8 (mm^3/(N m)) $\times 10^{-5}$). After being held for 6 h, the spheroidization of the PSPs reached its optimal level, with the shape factor (reflecting the degree to which the irregular particles approached a spherical shape) increasing from the original value of 0.39 to 0.78. High-temperature in situ confocal tests revealed that, during solid-solution treatment, Si atoms tend to migrate from regions of higher surface curvature to those of lower curvature, passivating the sharp corners of the PSPs and achieving spheroidization and refinement through multifaced growth. The refinement and spheroidization of the PSPs, as well as the lattice distortion induced by the solid-solution treatment, contributed to an increase in the hardness of the matrix, thus providing favorable conditions for the increased wear resistance of the GTSC A390 alloy. The present study provides new insight into optimizing PSPs in hypereutectic Al–Si alloys for industrial applications.

https://doi.org/10.1007/s11661-025-07898-y

I. INTRODUCTION

AL–SI alloys have been used in the automotive, aerospace and electronic packaging industries owing to their excellent casting properties, thermal conductivity, and specific strength.[1,2] With increasing in Si content, favorable conditions are provided for improving the wear resistance and thermal stability of Al–Si alloys,[3–5] promoting the wide application of hypereutectic Al–Si alloys (Si wt pct > 12.6 wt pct) in engine parts (such as pistons) and wear-resistant parts. The most distinguishing feature of hypereutectic Al–Si alloys compared with hypoeutectic Al–Si alloys is the presence of primary silicon particles (PSPs). Research has established that the size and morphology of PSPs critically affect the properties of hypereutectic Al–Si alloys.[6,7] In alloys produced via traditional casting methods, the microstructure typically consists of coarse PSPs, lamellar eutectic Si, and the α–Al phase. Notably, PSPs predominantly exhibit octahedral, plate-like, or five-petal star morphologies.[8–11] These geometric configurations are susceptible to stress concentrations at their sharp edges, ultimately resulting in matrix cracking and component failure. The coupled growth of the lamellar eutectic Si and α–Al phases affects the continuity of the alloy and reduces its plasticity. Furthermore, coupled growth hinders the migration of free electrons, thereby reducing the thermal conductivity of the alloy.[12,13] Therefore, in recent decades, refining the size and improving the morphology of Si phases in hypereutectic Al–Si alloys have become popular research topics.

Common refinement methods for PSPs in hypereutectic Al–Si alloys include ultrasonic treatment, semisolid treatment, rapid solidification and modification treatment. Ultrasonic treatment is an effective method

---

YUNA WU and CHENGCHENG HAN are with the College of Materials Science and Engineering, Hohai University, Changzhou 213200, P.R. China and also with the Suqian Research Institute, Hohai University, Suqian 223800, P.R. China. Contact e-mail: wuyuna@hhu.edu.cn ZONGHAN LI, YITONG HU, CHEN CHEN, JINGHUA JIANG and YONGHAO ZHAO are with the College of Materials Science and Engineering, Hohai University. Contact e-mails: yhzhao@njust.edu.cn, 20231179@hhu.edu.cn HENGCHENG LIAO is with the School of Materials Science and Engineering, Southeast University, Nanjing 211189, P.R. China.

Manuscript submitted January 14, 2025; accepted June 28, 2025.

for refining PSPs and improving the mechanical properties of hypereutectic Al–Si alloys.[14,15] This process relies mainly on applying high-energy ultrasonic waves to the melt, artificially increasing the number of nucleation sites, promoting the nucleation of PSPs and restricting their growth.[16–18] However, refining PSPs to sizes less than 20 μm solely via ultrasonic treatment is difficult and often requires additional processes, increasing complexity and cost. Semisolid treatment can significantly refine PSPs and improve their mechanical properties,[19,20] but it demands specialized equipment, precise cooling control, and skilled operation.

Rapid solidification can result in a very high cooling rate during solidification, allowing for a significant degree of undercooling and refinement in PSPs nucleation. In recent years, rapid laser solidification of Al–Si alloys has yielded positive outcomes.[21,22] However, the complexity of the processes involved and the high cost of equipment hinder its widespread adoption.

Modification is the primary method for refining the Si phase in Al–Si alloys, with Sr being the most common modifier. Modification transforms lamellar eutectic Si into fibrous and eventually spherical Si upon homogenization,[22–26] and promotes eutectic Si nucleation on PSPs by reducing structural supercooling.[27] While other modifiers such as Sb, Be, and P also aid in Si refinement,[28–33] their effects on PSPs are limited, and potential environmental risks must be considered.

The solidification of the hypereutectic Al–Si system shares strong similarities with that of the Fe–G (graphite) system, particularly in terms of coupled growth during eutectic solidification.[34] In nodular cast iron, the coupled growth of austenite (A) and flake graphite (GF) is replaced by the divorced growth of A and nodular graphite (GN).[35] Similarly, divorced eutectic growth of (Al + Si) can be achieved in hypereutectic Al–Si alloys via glass tube suction casting (GTSC) without any modifier, producing a unique microstructure of fine, discrete PSPs distributed within an α–Al matrix. Although the GTSC effectively refined PSP, the as-cast PSP retained faceted morphologies that are prone to stress concentration. Previous heat treatment studies have focused predominantly on eutectic Si spheroidization in coupled microstructures. However, PSPs evolution within divorced eutectic systems remains unexplored. Therefore, based on the divorced growth of the Al–Si hypereutectic alloy, this study achieves significant refinement, spheroidization of PSPs, and improvement in wear resistance through solid–solution treatment. With the aid of high-temperature in-situ confocal tests, this study further reveals the underlying mechanisms, offering valuable insights for future research.

II. EXPERIMENTS

In this study, commercial A390 alloy ingots were remelted in a self-designed resistance furnace. When it was kept in the molten state at 720 ± 5 °C for 30 half an hour, C_2Cl_6 with a melt mass of 0.8 pct was added for degassing and slag removal. The melt was then held at 650 °C for half an hour, after which the melted alloy was transferred to a glass tube (with a wall thickness of 1 mm and an inner diameter of 14 mm) and cooled in air. The actual chemical composition detected by a MAXx LMF15 optical emission spectrometer (OES) is shown in Table I (commercial A390 alloy). The commercial A390 alloy has a Si content of 16–18 wt pct, when C_2Cl_6 is used for melt degassing and slag removal, some material loss occurs, resulting in an actual Si content of 14.6 wt pct.

The microstructures of the samples were characterized by several instruments, including a BX60M optical microscope (OM), a HitachiS-3400N scanning electron microscope (SEM) and a Talos F200x transmission electron microscope (TEM) equipped with an energy dispersive spectrometer (EDS). Deep corrosion was induced with a 10 pct NaOH solution, whereas shallow corrosion was induced with a 0.5 pct HF solution. The phase compositions of the alloy samples were determined via X–ray diffraction (XRD) with a Bruker AXS D8 instrument. The samples were subjected to high-temperature in situ testing via an ultrahigh-temperature laser confocal microscope (VL2000DX-SVF18SP). Argon gas was introduced as a protective atmosphere to prevent oxidation during the testing process.

The average equivalent diameter (D) and shape fact (F) of the PSPs devices quantitatively determined via Image-Pro Plus image analysis software. These values were calculated according to Eq. [1][36]and Eq. [2]:[37]

$$D = \frac{\sum_{i=0}^{n} \sqrt{4A_i/\pi}}{n} \qquad [1]$$

$$F = \frac{\sum_{i=0}^{n} 4\pi A_i}{nL_i^2} \qquad [2]$$

where A_i is the area of a PSP, L_i is the perimeter of a PSP, and n is the total number of PSPs.

The GTSC A390 alloy was heat treated in a KSL-1100 X muffle furnace. According to the DSC curve of the A390 alloy,[38] the exothermic peak observed in the temperature range of 508.2 to 447.8 °C corresponds to the reaction of the Al_2Cu phase. In conjunction with various studies on the solid-solution treatment of Al–Si alloys,[39–42] this research determined the solid-solution treatment temperature to be 520 °C, with holding times of 2, 4, and 6 hours, to ensure that the majority of solute atoms were dissolved into the matrix.

The wear resistance of each sample was tested via an MS-T3000 friction and wear tester, as shown in Figure 1(b). The friction pair used in the wear resistance test consisted of a ZrO_2 ball indenter with a diameter of 5 mm rotating at a speed of 200 r/min under a load of 15 N for a test duration of 1 hour. The microhardness of the α-Al matrix was measured with a Vickers microhardness tester (HXD-1000TC). The friction and wear samples were weighed with an electronic scale with an accuracy of 0.0001 g, and the average mass loss was calculated. The calculation formula for the volume wear rate is Eq. [3]:[43]

$$W = \frac{W_m}{\rho \times F \times d} \qquad [3]$$

where W is the volume wear rate ($mm^3/(N\ m)$), W_m is the wear mass (mg), ρ is the material density (g/cm^3), F is the normal load (N) applied to the wear test, and d is the relative sliding distance (m) between the friction pair and the sample surface. The three-dimensional (3D) morphology of the wear scar was collected and processed via a 3D confocal white light interferometer (Sensofar Slynx 2).

III. RESULTS

A. *Microstructures of GTSC and Solution-Treated A390 Alloys*

The GTSC A390 Al–Si alloy exhibited a characteristic microstructure dominated by PSPs and α-Al, as well as some intermetallic Al_2Cu, as confirmed by the XRD pattern in Figure 2(a). Prominent peaks corresponding to crystalline Si and α-Al dominate the spectrum, whereas minor diffraction peaks at $2\theta = 29.385$ and 47.807 deg align precisely with the standard Al_2Cu phase, corroborating the presence of intermetallic compounds. This observation is further substantiated by the shallow-etched SEM micrograph [Figure 2(b)], where blocky bright regions (e.g., point c) are 68.4 at pct Al and 25.2 at pct Cu, aligning with the stoichiometric Al_2Cu composition, whereas needle-like features (e.g., point d) are consistent with the Al_5FeSi phases. These findings corroborate the established morphological and compositional benchmarks for the Al_2Cu and Al_5FeSi phases in previous reports.[37,44] Additionally, the microstructures of the GTSC A390 alloy include several Mg-rich phases and Mn-rich phases. As their contents are less than 1 wt pct, there are no corresponding characteristic peaks in the XRD results.

Table I. Actual Chemical Composition of the GTSC A390 alLoy (Wt Pct)

Alloy	Si	Cu	Fe	Zn	Mg	Mn	Al
A390	14.6	4.4	0.8	0.7	0.5	0.2	Bal.

The optical microstructures of the GTSC A390 alloys with different solid–solution treatment times are shown in Figures 3(a) through (d). These microstructures consisted of dark gray PSPs (blue arrows), an α-Al matrix (white arrow), and light gray intermetallic compounds (yellow arrows), such as blocky Al_2Cu. The PSPs in the unheated GTSC A390 alloy exhibit angular blocks, representing the two-dimensional morphology of the octahedral PSPs after polishing, with no visible lamellar eutectic Si; this is characteristic of a eutectic-divorced structure in a hypereutectic Al–Si alloy. The equivalent diameter histogram of Figure 3(e) indicates that most PSP systems have equivalent diameters ranging from 15 to 25 μm. After solid-solution treatment, the PSPs in the GTSC A390 alloy are significantly refined and uniformly distributed. The equivalent diameter histograms in Figures 3(f) through (h) indicate that most PSP systems have equivalent diameters between 2 and 8 μm. Figures 3(i), (j), (k) and (l) show the distributions of the scatter points representing the equivalent diameter and shape factor (*DF*) of the PSPs in the GTSC A390 alloy subjected to various solid–solution holding times. Each point corresponds to the equivalent diameter and shape factor a measured object, with the elliptical region indicating the high-density area. For untreated PSP systems, the *DF* distribution is widely scattered, with more than half of the *F* values falling below 0.4 and most diameters exceeding 10 μm, as shown in Figure 3(i). This finding suggests that the PSPs are coarse, unevenly distributed, and exhibit nonround morphologies. Following a 2-hour solid-solution holding [Figure 3(j)], the *DF*

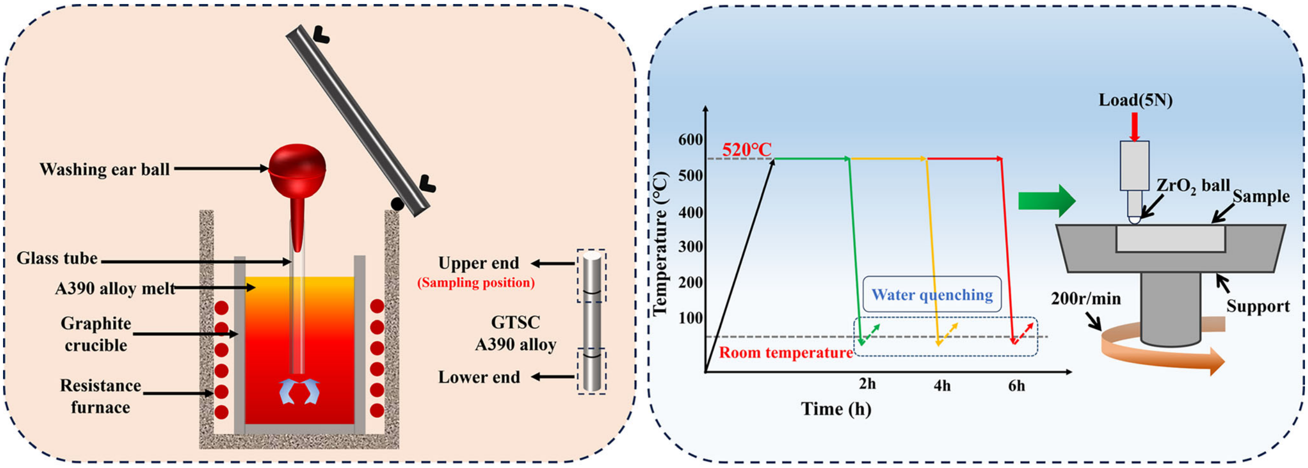

(a) (b)

Fig. 1—Experimental schematic: (*a*) glass tube suction casting[38] and (*b*) solid-solution treatment and wear test.

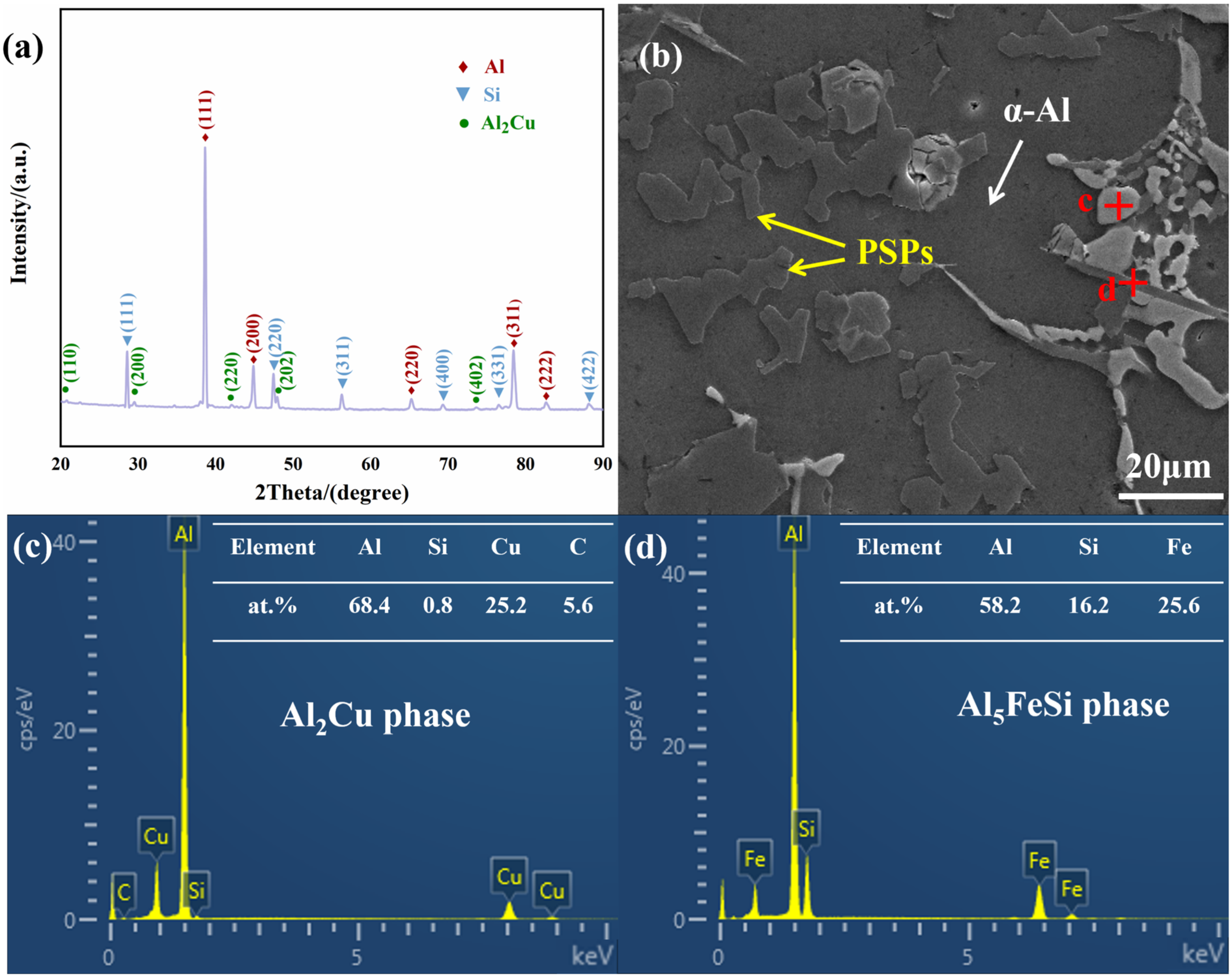

Element	Al	Si	Cu	C
at.%	68.4	0.8	25.2	5.6

Element	Al	Si	Fe
at.%	58.2	16.2	25.6

Fig. 2—Phase analysis of the GTSC A390 alloy: (*a*) XRD, (*b*) SEM, (*c*) EDS of point c in (b), and (*d*) EDS of point d in (b) (Color figure online).

scatter points shift leftward, indicating refinement, albeit with moderate roundness. With extended holding times of 4 hours [Figure 3(k)], the distribution becomes concentrated in the upper left quadrant, indicating smaller and rounder PSPs. Notably, after 6 hours of holding, although the majority of PSPs have F values exceeding 0.6, the number of PSPs with sizes greater than 15 μm also increased, as shown in Figure 3(l).

Figure 4(a) presents the average equivalent diameter and shape factor of the PSP mixture; with increasing solid–solution holding time, the size of the PSP mixture initially decreases but then increases. The average equivalent diameters of the PSPs after holding for 0, 2, 4, and 6 hours were 18.8, 6.5, 5.2, and 6.9 μm, respectively, and the shape factors were 0.39, 0.63, 0.75, and 0.78, respectively. The smallest PSPs, measuring 5.2 μm, occur with a holding time of 4 hours, after which they begin to coarsen with a 6 hours hold. As the holding time increased, the spheroidization effect became more pronounced, and the shape factor of the PSPs heated for 6 hours was 0.78. The average equivalent diameter of PSPs in GTSC A390 alloy decreased by 70.5 pct compared with that of the permanent mold casting A390 alloy in the previous study.[34] The refinement of the PSPs in the A390 alloy after solid-solution in the present work has achieved excellent results compared with those of other studies, as shown in Figure 4(b) and Table II.

B. *Morphology of the PSPs in the As-cast and Solution-Treated A390 Alloys*

Figure 5 shows the SEM morphology of the PSPs in the GTSC A390 alloy. The untreated PSPs appear angular, with a small number of coarse PSPs evident in Figure 5(a). At high magnification, some small PSPs are agglomerated, as depicted in Figure 5(b). Once the melt is sucked into the glass tube, a significant number of PSPs that are nucleated under the initial chilling become the nucleation centers for the remaining Si atoms in the melt.[38] At high degrees of undercooling, nonequilibrium solidification predominates, allowing the Si atoms in the residual melt to attach and grow at the leading edges of the already nucleated PSP.[34] This growth

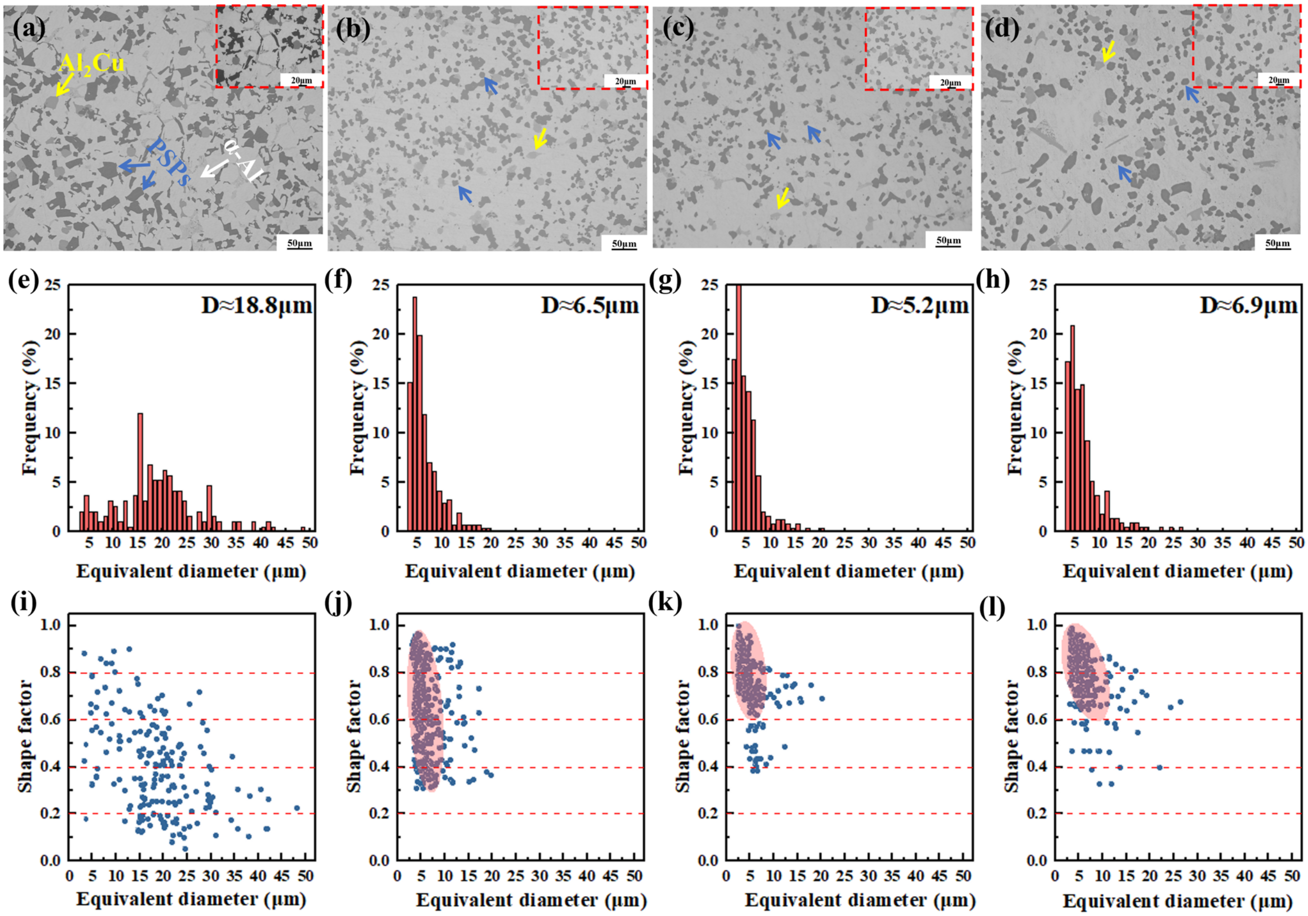

Fig. 3—Optical microstructures and equivalent diameter histograms of GTSC A390 alloys with different solid–solution holding times: (*a*), (*e*) 0 h, (*b*), (*f*) 2 h, (*c*), (*g*) 4 h, and (*d*), (*h*) 6 h; DF scatter point distributions of PSPs with different solid–solution holding times: (*i*) 0 h, (*j*) 2 h, (*k*) 4 h, and (*l*) 6 h.

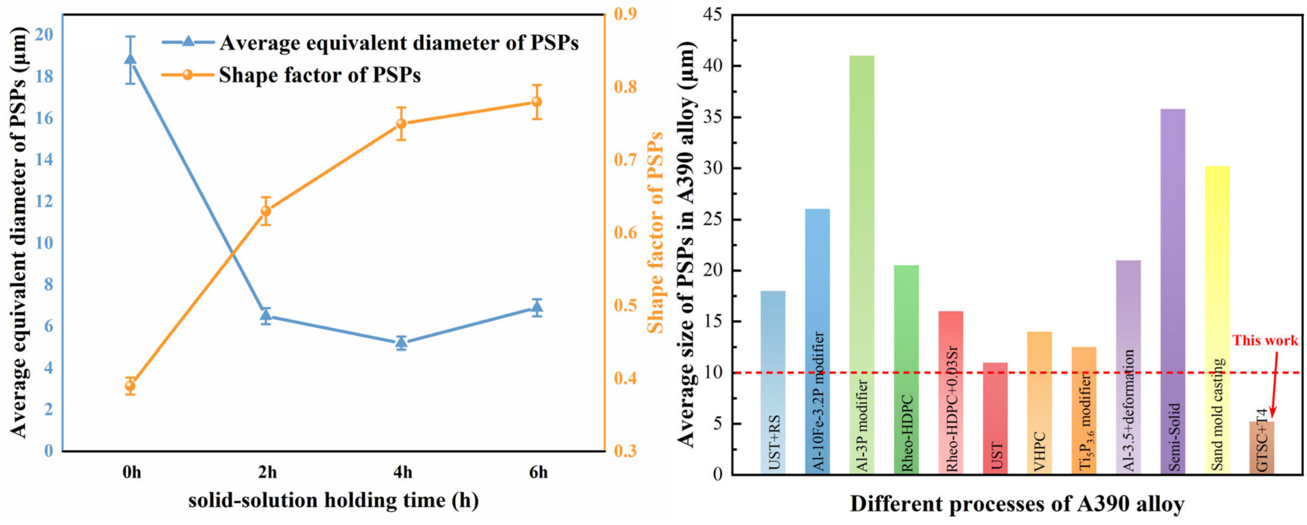

(a) (b)

Fig. 4—(*a*) Average equivalent diameters and shape factors of PSPs in GTSC A390 alloys with different solid–solution holding times; (*b*) size comparison of PSPs in A390 alloys produced by different processes and modifiers[27,34,45–51].

Table II. Size Comparison of PSPs in A390 Alloys Produced by Different Processes and Modifiers

Alloy	Process	Modifier	Average Size of PSPs (μm)	References
A390	**Glass tube suction casting**	—	**18.8**	**This work**
A390	**Glass tube suction casting + T4 (520 °C × 2 h)**	—	**6.5**	**This work**
A390	**Glass tube suction casting + T4 (520 °C × 4 h)**	—	**5.2**	**This work**
A390	**Glass tube suction casting + T4 (520 °C × 6 h)**	—	**6.9**	**This work**
A390	Ultrasonic melt treatment	Al-P	18	[45]
A390	Low pressure casting	Al-Fe-P	27	[46]
A390	Low pressure casting	Al-3P	41	[46]
A390	Rheo-HPDC	—	20.5	[27]
A390	Rheo-HPDC	0.03Sr	16	[27]
A390	Ultrasonic treatment + copper die casting	—	11	[47]
A390	Vacuum high pressure casting	—	14	[48]
A390	Permanent mold casting	Ti5P3.16	12.5	[49]
A390	Deformation	Al-3.5P	21	[50]
A390	Semi-solid	—	35.8	[51]
A390	Sand mold casting	—	30.2	[34]

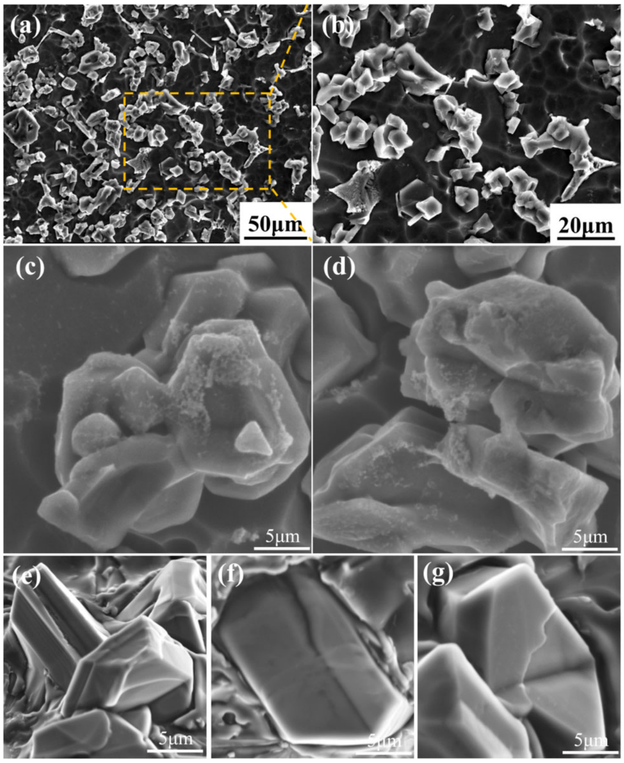

Fig. 5—SEM morphology of the PSPs in the untreated GTSC A390 alloy: (*a*), (*b*) overall morphology, (*c*), (*d*) overlapping PSPs, and (*e*), (*f*) and (*g*) twinned Si structures.

structure typically exhibits the phenomenon of multiple PSPs overlapping, as shown in Figures 5(c) and (d). In hypereutectic Al–Si alloys, PSPs display a unique growth mode known as the twin plane reentrant edge (TPRE). These twinned Si structures were also observed in the SEM image of the morphology of the untreated GTSC A390 alloy [Figures 5(e), (f), and (g)].

After solid-solution treatment, the PSPs are refined and spheroidized. However, the spheroidization effect of the PSPs after a 2 hours solid-solution hold is not very pronounced, because the overlap of the PSPs is still evident in Figures 6(a) and (d). This effect becomes more pronounced with longer holding times. After 4 and 6 hours [Figures 6(b) and (c)], the edges and corners of the PSP are noticeably passivated, which is a characteristic feature of spheroidization. The overlap of PSPs observed in the untreated samples and those held in the solid solution for 2 hours appeared to be reduced, resulting in evenly distributed fine PSPs, as shown in Figures 6(e) and (f). This observation aligns with the increase in the shape factor *F* corresponding to the duration of holding (see Figures 3 and 4).

C. *Wear Results*

Figure 7 shows the results of the wear tests. The serrations observed in Figure 7(a) arise from fluctuations in friction force, which are caused by changes in the smoothness and contact condition of the friction interface due to wear debris generation. These fluctuations reflect the typical three-stage wear process: an initial running-in stage with sharp changes due to asperity contact, a stable wear stage with smoother curves, and a severe wear stage where fluctuations increase again due to intensified wear and debris accumulation. The untreated sample shows an increasing trend in the friction coefficient after 30 minutes of sliding friction, indicating a transition into a severe wear stage. In contrast, the samples that underwent solid-solution treatment exhibited fluctuations in the friction coefficient of varying magnitudes after 30 minutes of sliding friction. The untreated sample has a relatively high friction coefficient of 0.337. For the solid-solution-treated samples, the friction coefficient decreases progressively from 0.266 (2 hours) to 0.251 (4 hours) and then increases slightly to 0.286 (6 hours). Figure 7(b) shows that the volume wear rate tends to be similar to that of the mean friction coefficient. The untreated sample has a relatively high mass wear rate of 55.5 ($\text{mm}^3/(\text{N m}) \times 10^{-5}$). In contrast, the mass wear rates of the samples subjected to solid-solution

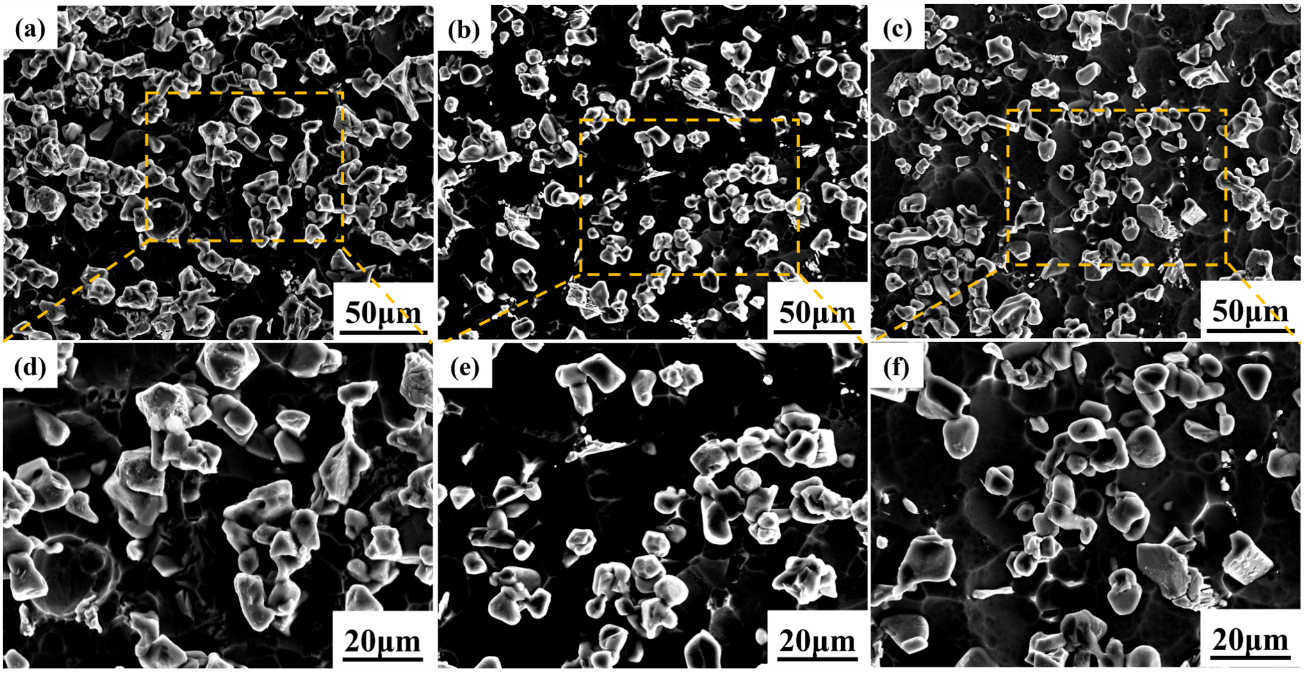

Fig. 6—SEM morphology of PSPs in GTSC A390 alloys with different solid–solution holding times: (*a*), (*d*) 2 h, (*b*), (*e*) 4 h, and (*c*), (*f*) 6 h.

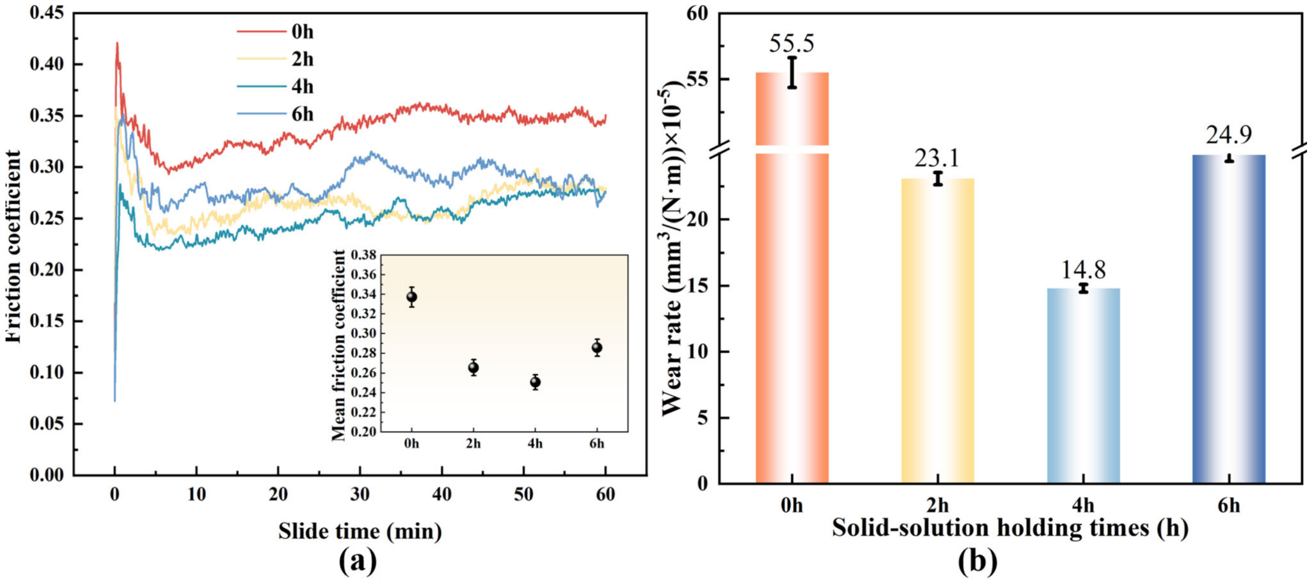

Fig. 7—Friction curves and wear rates of the GTSC A390 alloy with different solid–solution holding times: (*a*) friction curves and (*b*) wear rates (Color figure online).

treatment tended to decrease: 23.1 (mm^3/(N m)) × 10 5) for a holding time of 2 hours, decreased to 14.8 (mm^3/(Nm)) × 10^{-5}) for 4 hours, and then increased to 24.9 (mm^3/(Nm)) × 10^{-5}) for a holding time of 6 hours. Combined with the previously mentioned size variation of PSPs (Figures 3 and 4), it can be deduced that smaller PSPs result in better wear resistance.

Figure 8 shows the three-dimensional (3D) morphology of the wear scars after testing. The untreated sample exhibited a dark, elongated line in the center of the wear scar, representing a groove, as shown in Figure 8(a). In contrast, the 3D wear scars of the samples subjected to solid-solution treatment show minimal variation, as depicted in Figures 8(b), (c), and (d). However, when the width and depth of the wear scars were quantified, significant differences emerged between the untreated samples and those that underwent solid-solution treatment, with additional variations observed among samples with different holding times, as detailed in Figure 9. The wear scar profile of the untreated sample is V shaped, with a maximum wear depth of 46.16 μm and a mean wear depth of 25.15 μm. In contrast, the wear scar

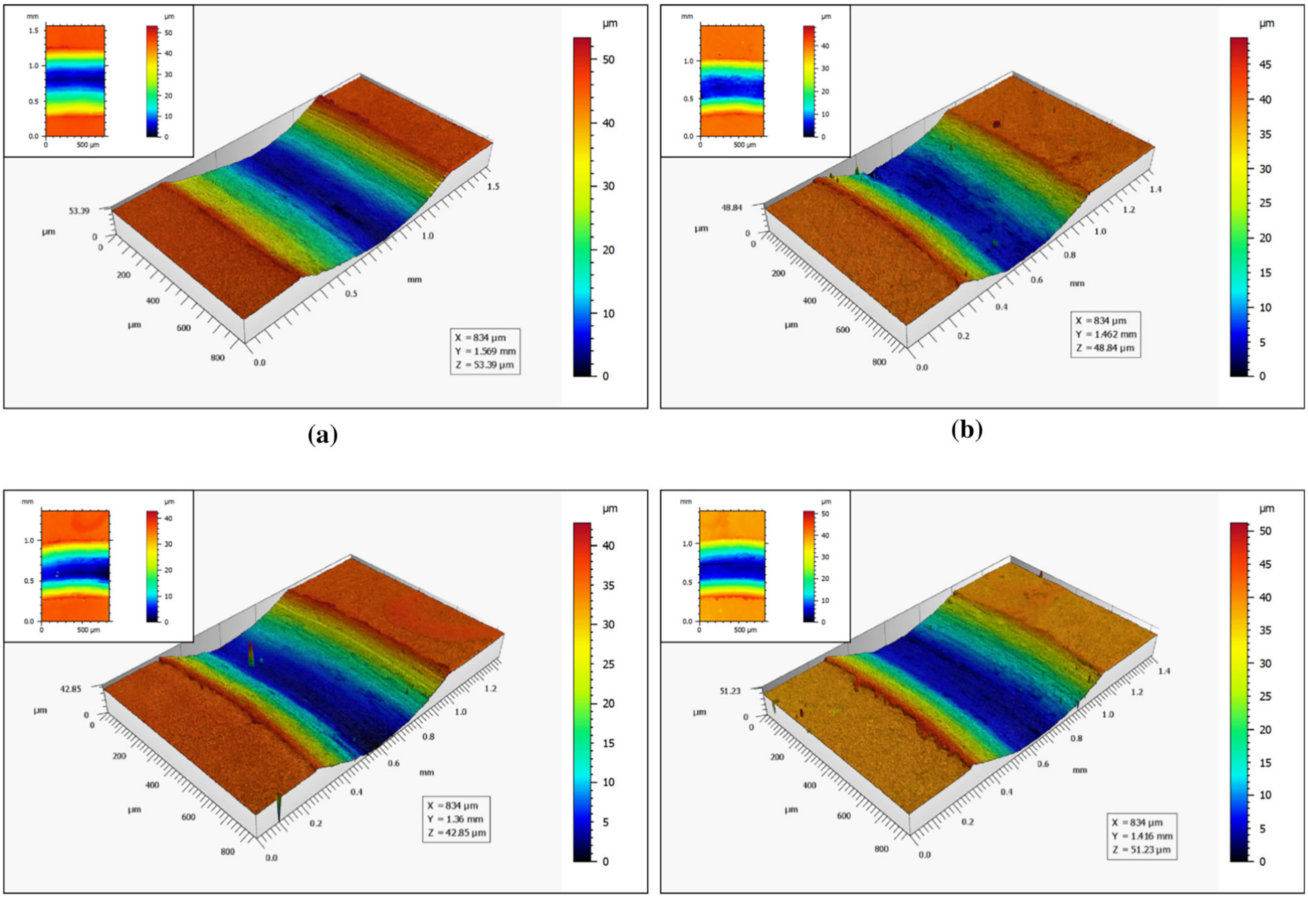

(a) (b)

(c) (d)

Fig. 8—3D topography of the wear scars on GTSC A390 alloys with different solid–solution holding times: (*a*) 0 h, (*b*) 2 h, (*c*) 4 h, and (*d*) 6 h (Color figure online).

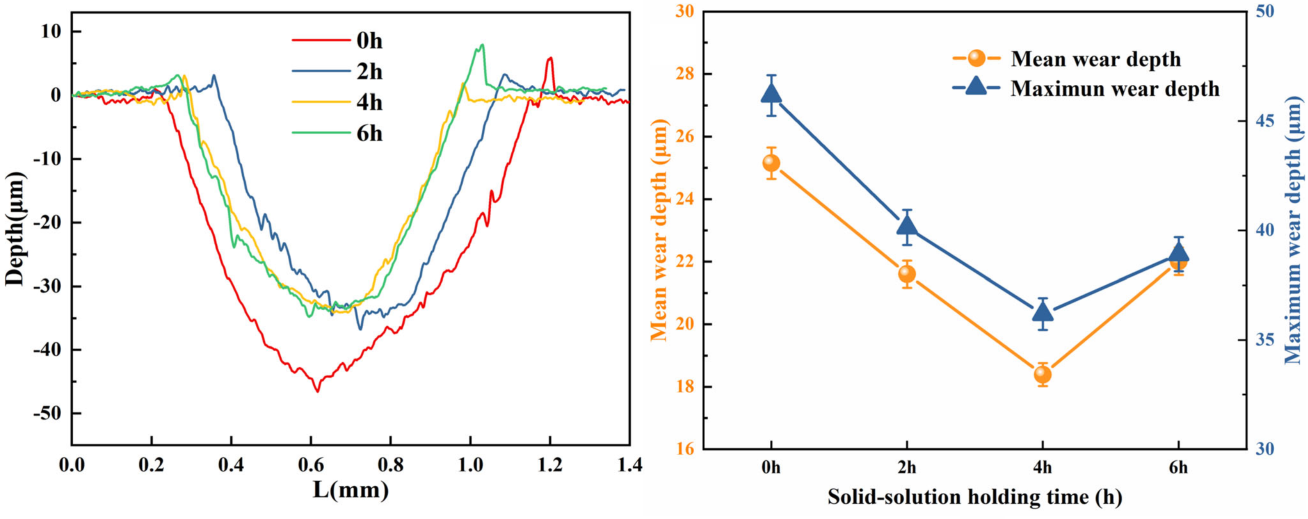

(a) (b)

Fig. 9—Wear scar measurement results: (*a*) 2D wear scar profiles and (*b*) wear depth (Color figure online).

profiles of the samples after solid-solution treatment are U shaped. As the holding time increased (2, 4, and 6 hours), the maximum wear depth (40.13, 36.18, and 38.91 μm) and mean wear depth (21.6, 18.39, and 22.01 μm) initially decreased but then increased. These results are consistent with the variations in the friction

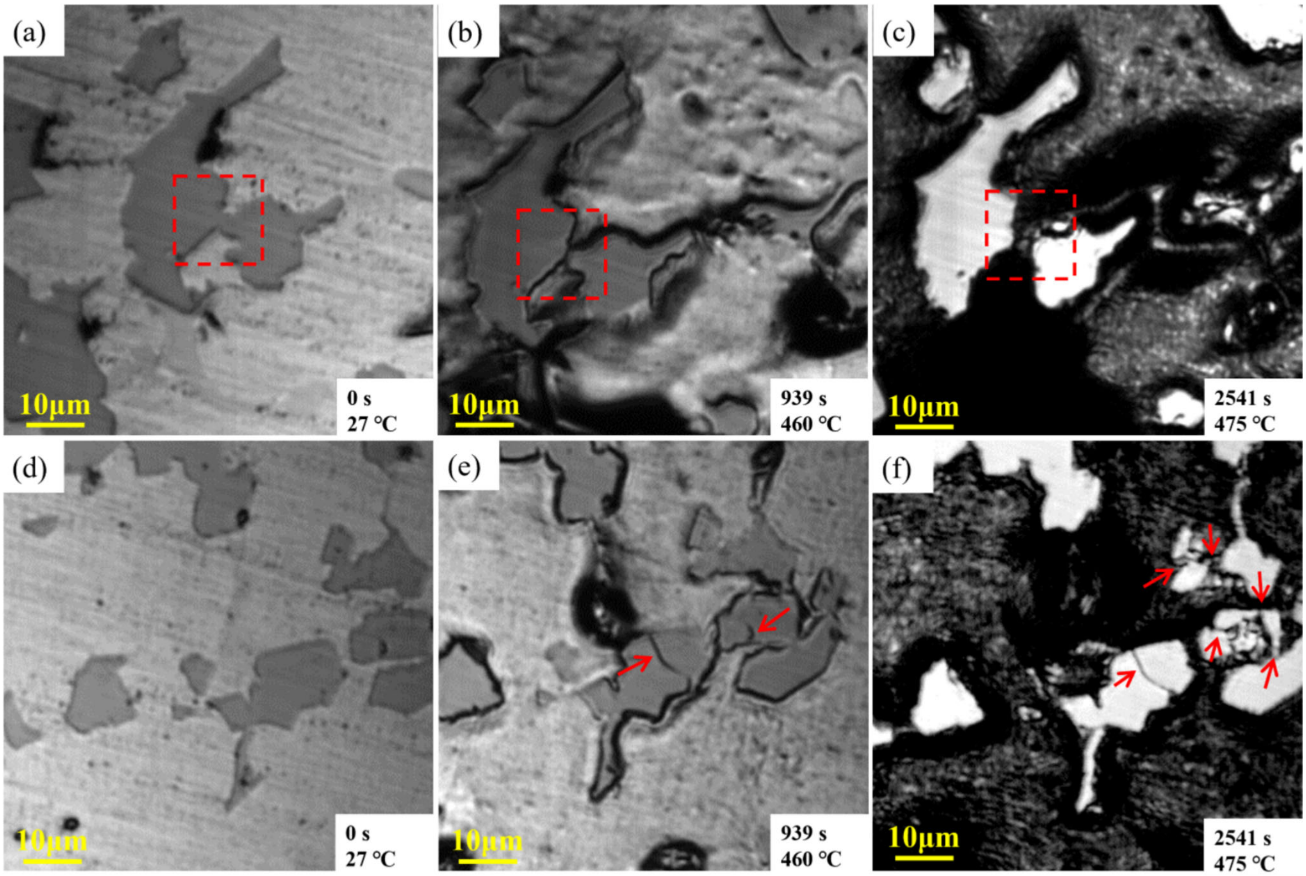

Fig. 10—High-temperature in-situ test of GTSC A390 alloy: (*a*), (*d*) 27 °C; (*b*), (*e*) 460 °C; (*c*), (*f*) 475 °C.

curves and the mass wear rate, indicating that smaller PSPs result in increased wear resistance.

IV. DISCUSSION

A. *Refinement Analysis of PSPs*

To better observe the changes in PSPs at high temperatures, in-situ confocal microscopy was performed on the GTSC A390 alloy. Owing to the negative chamber pressure lowering the melting point, the observation temperature was maintained at 460–480 °C. PSPs appear dark at room temperature and 460 °C and turn bright white at 475 °C. In this study, the refinement of the PSPs in the GTSC A390 alloy due to solid-solution treatment can be attributed to two main factors. First, overlapping PSPs in GTSC A390 tend to separate into multiple independent particles at elevated temperatures. Second, at elevated temperatures, Si atoms dissolve into the matrix, reducing the size of the PSPs.

Figure 10(a) shows the typical two-dimensional morphology of PSPs, where two or several PSPs overlap, a phenomenon also observed in the three-dimensional morphology of the PSPs in Figures 5(a) and (b). Under high-magnification SEM, smaller PSPs tend to agglomerate around larger PSPs. This phenomenon is not surprising in the microstructure of the eutectic-divorced sample. When the A390 alloy melt is sucked into the glass tube, the initial chilling effect (83.7 °C/s)[38] and vigorous filling induce a large amount of nucleation of PSPs; this depletes the remaining melt of Si atoms, which is well below the eutectic composition point, thus preventing a normal eutectic reaction and forming a eutectic-divorced structure. The Si atoms are then forced to grow by adhering to the already nucleated PSPs, forming Si atom clusters around them. Once these clusters reach the critical nucleation radius, they nucleate. As a result, this overlapping pattern is observed in the characterization results. The overlapping regions of PSPs exhibit high degrees of distortion and weak thermal stability,[52–56] resulting in their eventual separation at elevated temperatures as the holding time increases, as indicated by the red dashed box in Figures 10(b) and (c). This factor is one of the reasons for the observed PSP refinement.

As shown in Figures 10(d) and (e), with increasing temperature, cracks (indicated by red arrows) were observed in several intact PSP systems. The coarse PSPs tend to segment into multiple smaller PSPs[13,39–41] [Figure 10(f)], which is then followed by partial dissolution into the Al matrix. Consequently, the average equivalent diameter naturally decreases when the PSP size is measured; this represents another reason for the refinement of PSPs during solid-solution treatment, which is closely related to the enrichment of solute atoms.

During the nucleation and growth of PSPs, twin formation on {111} planes produce growth grooves.[57] As the degree of undercooling decreases, the growth mode of these planes transitions from unidirectional growth to faceted growth.[58–60] Figures 5(e) through (g) show three typical twin PSPs formed via the TPRE growth mechanism. These grooves cause lattice distortion within the matrix, acting as primary diffusion channels for solute atoms, which enables their enrichment during solidification. At elevated temperatures, the enriched solute atoms at these grooves preferentially melt, resulting in the separation of complete twin PSPs into multiple smaller PSPs. Furthermore, solute atoms can also accumulate at the overlap regions of PSPs or at grain boundaries. These solute-enriched regions exhibit relatively low diffusion activation energies,[61] which increases the diffusion tendency of solute atoms. At high temperatures, the solubility of Si atoms in the α-Al matrix increases, allowing them to easily dissolve into the matrix with the solute atoms, thereby reducing the size of the PSPs.

B. *Spheroidization Analysis*

The spheroidization mechanism of the solid solution treatment of PSP is mainly separation and dissolution. GTSC is a type of nonequilibrium solidification, and the PSPs in the A390 alloy are not completely grown. Owing to the inhomogeneous surface curvature and lattice distortion energy, the solid solubility of PSPs in the α-Al matrix varies throughout. The relationship between the solid solubility of PSPs in the equilibrium α-Al matrix and the surface curvature is[62]:

$$ln\frac{C(K,\mu_d)}{C}=\frac{2\sigma K\overline{V}}{RT}+\frac{\mu_d}{RT} \qquad [4]$$

where C is the solubility of the complete planar Si in the equilibrium α-Al matrix; $\overline{V}$ is the partial molar volume of Si, cm^3/mol; σ is the interface energy between α-Al and PSPs; R (1.987 Cal/mol*K^{-1}) is the gas constant; T is the absolute temperature, K; μ_d is the lattice distortion energy of unit molar Si atom, Cal/mol; and K is the surface curvature of PSPs, cm^{-1}. Because the surface curvature and lattice distortion energy of the tip and edge of the PSP are typically greater than those of the passivation region, the equilibrium solute concentration is greater.

According to Eq. [4], Si atoms tend to diffuse from regions of high surface curvature, such as the tips and edges of PSPs, toward regions of lower curvature,[63] passivating sharp corners [Figures 11(a) and (b)] and reducing the interfacial and total system energy. This spontaneous process lowers the system free energy and provides a driving force for Si atom redistribution. This process is the result of Si atoms dissolving from regions of high distortion energy and diffusing toward regions of lower distortion energy, essentially representing the transfer of Si atoms.

During solid-solution treatment, Si atoms dissolve from regions with high distortion energy (e.g., tips, edges, and overlap zones of PSPs) and diffuse toward areas with lower energy, facilitating size and shape changes. Compared with PSP, eutectic Si has greater surface curvature and distortion energy differences, making the spheroidization of eutectic Si more pronounced and widely explored.

In the divorced eutectic structure, PSP overlap increases the local distortion energy, improving silicon transfer. As shown in Figures 11(b) and (c), with prolonged holding time, necked or connected PSP

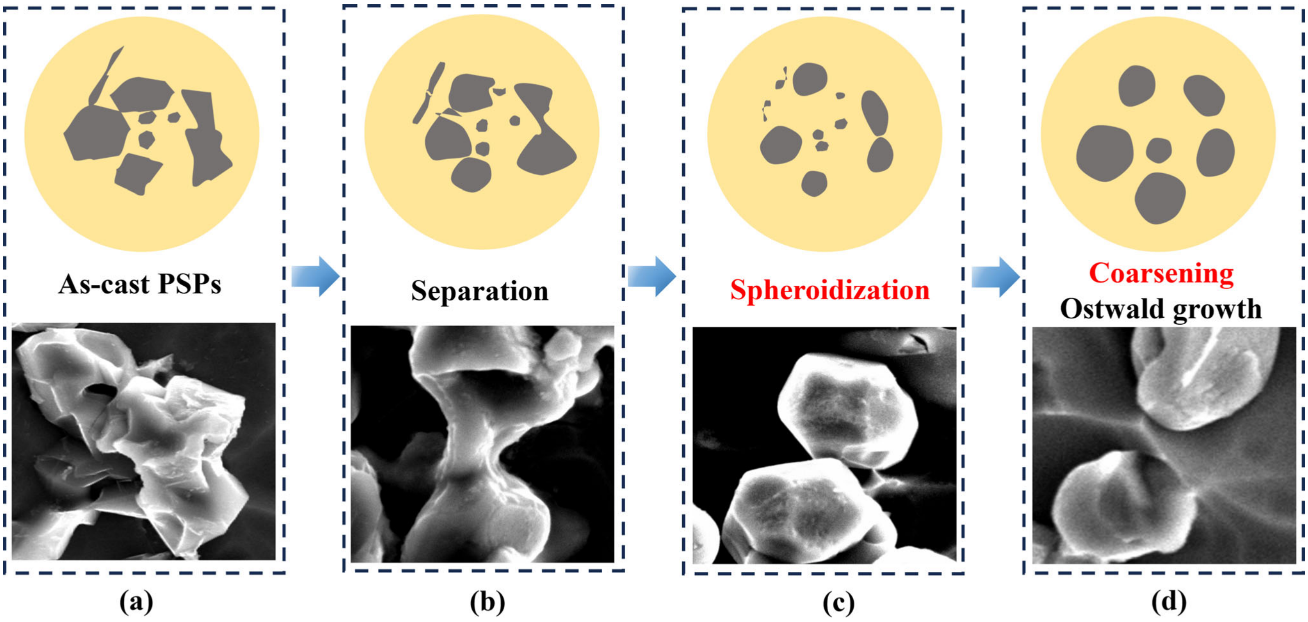

Fig. 11—Spheroidization mechanism diagram of PSPs.

regions undergo separation.[64–66] Continued diffusion causes local solute depletion around smaller PSPs and supersaturation around larger PSPs. To reduce the interfacial energy,[67] multidirectional growth promotes spheroidization [Figure 11(c)].

Once solute diffusion approaches equilibrium, PSPs coarsen and grow via Ostwald ripening.[68] Size-dependent equilibrium concentrations create concentration gradients, causing smaller PSPs to shrink or disappear, whereas larger PSPs grow and merge [Figure 11(d)]. This finding explains the increased coarsening and spheroidization of PSPs after 6 h of treatment compared with those after 2 or 4 hours of treatment.

C. *Wear Resistance Analysis*

After solid-solution treatment of the GTSC A390 alloy, significant changes in the morphology and size of the PSPs inevitably affect the material performance. Moreover, the hardness of the α-Al matrix, as the primary wear-bearing phase, plays a crucial role in the wear resistance. As shown in Figure 12(a), solid-solution treatment increased the matrix microhardness, and this effect increased with increasing holding time. Studies have shown that increased hardness is positively correlated with enhanced wear resistance.[69–72] According to the XRD results in Figure 12(b), the characteristic peak of the α–Al phase on the (111) crystal plane after solid-solution treatment clearly shifted, indicating a change in the spacing of the crystal plane. The angle between the X-ray and the (111) crystal plane has been altered.[73] According to the Bragg equation theory, the formula for calculating the crystal plane constant is derived Eq. [5].[74]

$$a = \frac{\lambda\sqrt{h^2 + k^2 + l^2}}{2\sin\theta} \qquad [5]$$

where a is the lattice constant, nm; λ is 0.15405 nm; (hkl) represents Miller indices (111); and θ represents the grazing angle.

The lattice constants of α–Al on the (111) plane of the GTSC A390 alloy were calculated to be 0.42698, 0.42742, 0.42823, and 0.42870 nm after different solution treatment times of 0, 2, 4, and 6 hours, respectively. The lattice constant of α–Al at room temperature is 0.40496 nm.[75]

The GTSC A390 alloy exhibited significant lattice distortion due to nonequilibrium solidification. EDS mapping of the TEM images [Figure 13(a)] reveals solute atoms such as Zn and Cu dissolved in the α-Al matrix, as well as numerous entangled dislocations. Solid-solution treatment further increases solute atom dissolution.[76] High-temperature in situ observations [Figures 13(b) through (d)] revealed that intermetallics rich in Fe, Cu, and Mg gradually melted and dissolved into the α-Al matrix with increasing temperature. This process leads to a reduction in the volume fraction of hard phases such as Al_2Cu, resulting in a decrease in the overall hardness of the alloy.[77] However, these solute atoms and dislocations intensify lattice distortion, which increases the matrix hardness[78,79] and resistance to plastic deformation. A harder matrix provides a mechanically stable substrate, reducing tangential wear damage and ultimately increasing wear resistance.[80]

Based on the friction curves and wear rate results, the sample subjected to solid-solution treatment for 4 hours, rather than the sample with the highest matrix hardness that underwent solid-solution treatment for 6 hours, exhibited the best wear resistance. This finding demonstrated that, in this study, the size and morphology of the PSPs were the primary factors influencing wear resistance. SEM images of the worn surfaces of the GTSC A390 alloy are shown in Figure 14. Many spalling, deep grooves and microcracks appear on the

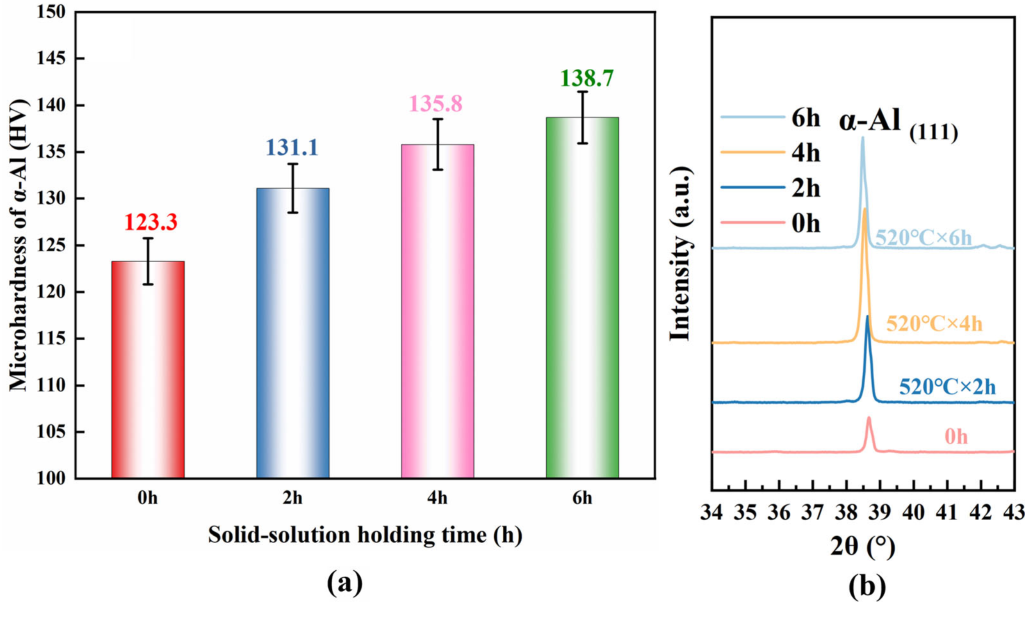

Fig. 12—Microhardness (*a*) and XRD results (*b*) of the α-Al matrix of the GTSC A390 alloys at different solid–solution holding times.

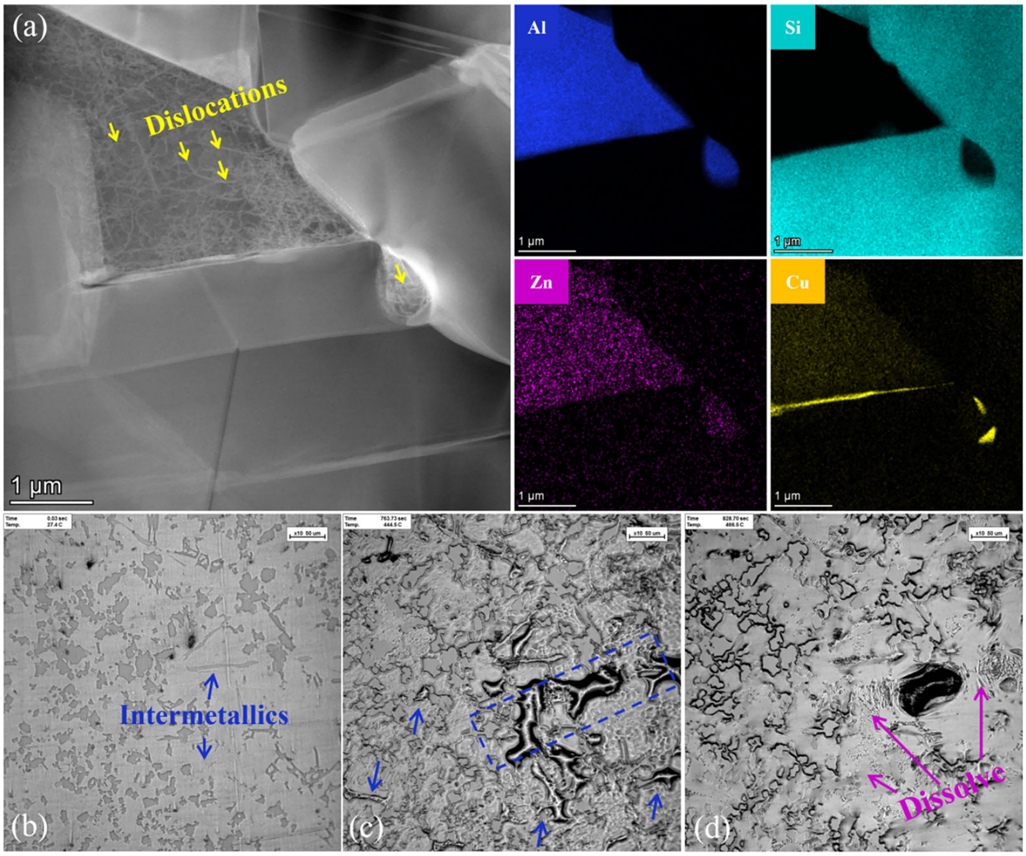

Fig. 13—TEM image with EDS mapping and high-temperature in-situ test of the GTSC A390 alloy: (*a*) TEM and EDS; (*b*), (*c*) and (*d*) high-temperature in-situ test.

worn surface of the unheated sample, as depicted in Figure 14(a). The coarse PSPs are prone to breaking during the wear process, which causes them to spall from the matrix and act as abrasives. This characteristic results in deep grooves, which are indicative of typical abrasive wear. If the debris are not removed continuously, the wear will then be a three-body interaction.[81] Furthermore, partial plastic deformation can be observed (marked by pink arrows), which is characteristic of adhesive wear. Thus, the wear mechanism of the untreated GTSC A390 alloy includes both abrasive wear and adhesive wear. The worn surface morphology of the GTSC A390 alloy improved after 2 and 4 hours of solid-solution treatment, with fewer and shallower grooves, fewer spalling pits, and a smoother friction oxide layer, as shown in Figures 14(b) and (c). The EDS results in Figure 14(c) confirmed that oxidation occurred during the wear process. The oxide layer is beneficial for blocking the actual contact between the two friction surfaces, providing lubrication, reducing the friction coefficient, and decreasing the wear rate. However, after 6 hours of solid-solution treatment, the delaminated area and pit size increased, whereas the number of grooves decreased, as shown in Figure 14(d). Therefore, the main wear mechanism of the GTSC A390 alloy after solid–solution treatment is abrasive wear.

Most of the PSPs in untreated samples are octahedral and exist in the matrix as discrete particles.[9,11,33] Therefore, the bonding strength between the PSPs and the matrix is relatively low, and the interface area between the PSPs and the matrix is very prone to cracking and spalling.[82,83] In addition, the sharp edge of the PSP tip introduces a serious stress concentration effect in the alloy matrix,[69,84] resulting in deep grooves during the wear process. Moreover, the PSPs in the A390 alloy are brittle. Under the action of an external force, once the initiated cracks combine with each other during the propagation process, PSPs will inevitably fall off from the matrix. These spalled PSPs act as wear debris, which also aggravates the wear of the matrix, increasing the wear rate and decreasing the wear resistance. The improvement in the wear resistance of the A390 alloy after solid–solution treatment is inseparable from the effects of the refinement and spheroidization of the PSPs. These uniformly distributed fine PSPs increase the overall load carrying capacity and effectively reduce the local stress concentration in the matrix,[85] thereby inhibiting the propagation of cracks between the PSPs and α-Al. The number of delaminated PSPs in the GTSC A390 alloy is reduced, thus increasing the overall wear resistance.

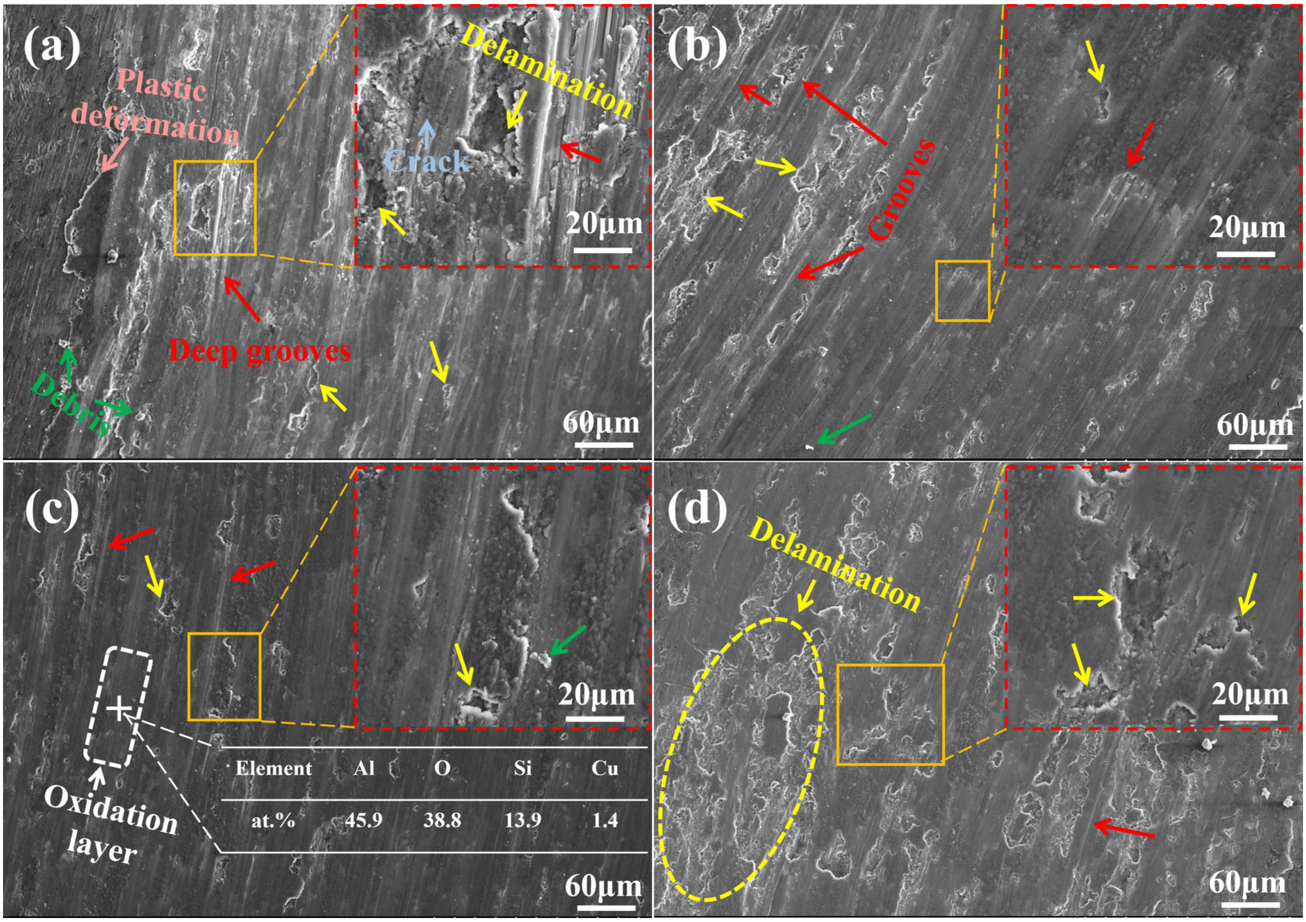

Fig. 14—SEM worn surfaces of GTSC A390 alloys with different solid–solution treatment times: (*a*) 0 h, (*b*) 2 h, (*c*) 4 h, and (*d*) 6 h.

V. CONCLUSIONS

In this study, GTSC combined with solid-solution treatment were employed to refine and spheroidize PSPs efficiently in a eutectic-divorced hypereutectic Al-Si alloy (A390), resulting in increased wear resistance. The main conclusions are summarized as follows:

1. The solid-solution treatment at 520 °C for 4 hours yielded the finest PSPs (from 18.8 to 5.2 μm) and significantly reduced the wear rate (from 55.5 to 14.8 $(\mathrm{mm}^3/(\mathrm{N\ m})) \times 10^{-5}$)). The 6 h treatment resulted in the highest shape factor (from 0.39 to 0.78), indicating effective spheroidization.
2. PSP refinement can be attributed to separation of overlapping PSPs formed during eutectic-divorced solidification and dissolution of Si atoms into the Al matrix in solute-rich regions.
3. Spheroidization was driven by separation and dissolution, where Si atoms diffused from high- to low-curvature regions, smoothing sharp features and promoting rounded morphologies.
4. Lattice distortion caused by solute atom dissolution increased the matrix hardness, whereas refined and spheroidized PSPs reduced the stress concentration and crack propagation during wear, resulting in increased wear resistance.

ACKNOWLEDGMENTS

The authors would like to acknowledge the financial supports of the Fundamental Research Funds for the National Natural Science Foundation of China (52303390), Jiangsu Provincial Key Research and Development Program (BE2021027), Postgraduate Research & Practice Innovation Program of Jiangsu Province (SJCX24_0194), Jiangsu Provincial Engineering Research Center for Structure-Function Integrated Metallic Materials for Harsh Environments, and Innovation Center for Critical Materials in Hydraulic Infrastructure Safety and Water Environment Restoration Hohai University.

AUTHOR CONTRIBUTIONS

Yuna Wu: conceptualization, writing-review & editing, methodology, funding acquisition. Chengcheng Han: data curation, writing-original draft, investigation. Zonghan Li: software, investigation. Yitong Hu: investiagation, formal analysis. Chen Chen: formal

analysis, data curation. Jinghua Jiang: methodology, supervision. Hengcheng Liao: methodology, supervision. Yonghao Zhao: conceptualization, supervision.

DATA AVAILABILITY

The data that support the findings of this study are available on request from the corresponding author.

CONFLICT OF INTEREST

The authors declare that they have no known competing financial interests or personal relationships that could have appeared to influence the work reported in this paper.

SUPPLEMENTARY INFORMATION

The online version contains supplementary material available at https://doi.org/10.1007/s11661-025-07898-y.

REFERENCES

1. K. Godbole, B. Bhushan, S.V.S. Narayana Murty, and K. Mondal: *Prog. Mater. Sci.*, 2024, vol. 144, p. 101268.
2. Y.Q. Han, D.X. Zhang, Z.B. Sun, Z. Liu, and Y.C. Xing: *J. Inner Mongolia Univ. Technol. (Nat. Sci. Ed.)*, 2024, vol. 43, pp. 467–74.
3. G.D. Wang, T. Hua, J.P. Yao, S.Y. Chen, J.Y. Cao, and Y.R. Zhou: *J. Alloy. Compd.*, 2025, vol. 1010, 177746.
4. Y.N. Wu, H.C. Liao, J. Yang, and K.X. Zhou: *J. Mater. Sci. Technol.*, 2014, vol. 30, pp. 1271–77.
5. W.X. Fan, H. Liu, Y.N. Wu, J.H. Jiang, and A.B. Ma: *J. Mod. Transp. Metall. Mater.*, 2025, vol. 5, pp. 86–100.
6. C. Ding, H.L. Hao, Z.G. Lu, C.Y. Yu, X.Z. Wu, P. Yu, and S.L. Ye: *Mater Charact*, 2023, vol. 202, 113026.
7. Y.H. Lee, S.H. Kayani, J.M. Lee, S.I. Lee, S.J. Kim, J.I. Jang, and Y.H. Cho: *J. Alloy. Compd.*, 2024, vol. 1008, 176580.
8. G. Zimmermann, C. Pickmann, and E. Schaberger Zimmermann: *J. Cryst. Growth*, 2022, vol. 585, 126589.
9. L.X. Xi, S. Guo, K. Ding, K.G. Prashanth, B. Sarac, and J. Eckert: *Vacuum*, 2021, vol. 191, 110405.
10. Y.J. Xu, Y. Deng, D. Casari, R.H. Mathiesen, and Y.J. Li: *J. Alloy. Compd.*, 2020, vol. 832, 154948.
11. J. Wang, Z. Guo, and S.M. Xiong: *Mater Charact*, 2017, vol. 123, pp. 354–59.
12. P. Ma, Z.J. Wei, Y.D. Jia, Z.S. Yu, K.G. Prashanth, S.L. Yang, C.G. Li, L.X. Huang, and J. Eckert: *J. Alloy. Compd.*, 2017, vol. 709, pp. 329–36.
13. K. Li, J. Zhang, X.L. Chen, Y.H. Yin, Y. He, Z.Q. Zhou, and R.G. Guan: *J. Mater. Res. Technol.*, 2020, vol. 9, pp. 8780–86.
14. N. Balasubramani, J. Venezuela, D. Stjohn, G. Wang, and M. Dargusch: *J. Mater. Sci. Technol.*, 2023, vol. 144, pp. 243–65.
15. N. Balasubramani, G. Wang, D.H. Stjohn, and M.S. Dargusch: *J. Mater. Sci. Technol.*, 2021, vol. 65, pp. 38–53.
16. J.G. Jung, J.M. Lee, Y.H. Cho, and W.H. Yoon: *J. Alloy. Compd.*, 2017, vol. 693, pp. 201–10.
17. Q.Q. Li, W.M. Jiang, Y.C. Xu, L.H. Yu, Y.Q. Niu, and Z.T. Fan: *J. Mater. Sci. Technol.*, 2024, vol. 197, pp. 78–93.
18. M.F. Qi, Y.Z. Xu, J.Y. Li, Y.L. Kang, and Z. Wulabieke: *Corros. Sci.*, 2021, vol. 180, 109180.
19. C. Liang, Z.H. Chen, Z.Y. Huang, and F.Q. Zu: *Mater. Sci. Eng. A*, 2017, vol. 690, pp. 387–92.
20. G.D. Ma, L. Li, S.Y. Xi, Y. Xiao, Y.K. Li, Z.T. Yuan, Y.H. He, R.F. Zhou, and Y.H. Jiang: *Mater Charact*, 2021, vol. 176, 111143.
21. H.H. Lien, J. Mazumder, J. Wang, and A. Misra: *Mater. Rech. Lett.*, 2020, vol. 8, pp. 291–98.
22. A. Bobel, Y.J. Kim, R. Maddalena, and A.K. Sachdev: *Mater. Sci. Eng. A*, 2024, vol. 901A, 146549.
23. A. Ghosh, W.Q. Wu, B.P. Sahu, J. Wang, and A. Misra: *Mater. Sci. Eng. A*, 2023, vol. 885A, 145648.
24. J. Zhang, J.R. Chen, H.M. Chen, L. Wang, Y. Zhang, R. Li, and B.B. Chen: *Mater Charact*, 2022, vol. 194, 112348.
25. K. Shiga, Y. Murakami, H. Harada, and N. Omura: *Metall. Mater. Trans. A*, 2024, vol. 55A, pp. 967–81.
26. Y.N. Wu, C.M. Liu, H.C. Liao, J.H. Jiang, and A.B. Ma: *J. Alloy. Compd.*, 2021, vol. 856, 158072.
27. P.Y. Yan, W.M. Mao, J. Fan, B.K. Wang, and Y.B. Liu: *J. Alloy. Compd.*, 2020, vol. 835, 155297.
28. C. Li, F. Liu, F. Yu, H. Qiao, D. Zheng, and Q. Le: *J. Mater. Res. Technol.*, 2023, vol. 23, pp. 1204–13.
29. C.L. Pereira, L.F. Gomes, A. Garcia, and J.E. Spinelli: *J. Alloy. Compd.*, 2021, vol. 878, 160343.
30. P. Tang, Q.N. Liu, F.Y. Yu, F. Mo, and L.M. Qin: *J. Alloy. Compd.*, 2023, vol. 931, 167478.
31. C.Y. Li, F. Liu, J.Q. Yin, F.X. Yu, D.P. Zheng, H.R. Qiao, Y.J. He, and Q.C. Le: *J. Alloy. Compd.*, 2024, vol. 1012, 175167.
32. L. Zhang, S.Y. Chen, Q.C. Li, and G.W. Chang: *Mater. Des.*, 2020, vol. 193, 108853.
33. X.Z. Zhu, S.H. Wang, X.X. Dong, X.F. Liu, and S.X. Ji: *J. Mater. Sci. Technol.*, 2022, vol. 100, pp. 36–45.
34. H.C. Liao, Y.N. Wu, H. Chen, and L.J. Qian: *Metall. Mater. Trans. A*, 2022, vol. 53A, pp. 2346–50.
35. M.F. Zhu, L. Zhang, H.L. Zhao, and D.M. Stefanescu: *Acta Mater.*, 2015, vol. 84, pp. 413–25.
36. D. Wang, C.C. Jiang, G.Y. Cai, J. Li, Y.B. Hui, Y.G. Guo, and F.H. Ba: *J. Mater. Eng. Perform.*, 2025, vol. 34, pp. 2681–89.
37. M.F. Qi, Y.L. Kang, Y.Z. Xu, Z. Wulabieke, and J.Y. Li: *Mater. Sci. Eng. A*, 2020, vol. 776, 139040.
38. C.C. Han, Y.N. Wu, H. Huang, C. Chen, H. Liu, J.H. Jiang, A.B. Ma, J. Bai, and H.C. Liao: *Acta Metall. Sin. (Engl. Lett.)*, 2024, vol. 37, pp. 2094–2105.
39. Y.C. Lin, S.C. Luo, J. Huang, L.X. Yin, and X.Y. Jiang: *Mater. Sci. Eng. A*, 2018, vol. 725A, pp. 530–40.
40. S.S. Dash, D.J. Li, X.Q. Zeng, D.Y. Li, and D.L. Chen: *Mater. Sci. Eng. A*, 2023, vol. 866A, 144283.
41. N. Zhao, H.J. Ma, Z.L. Hu, Y. Yan, and T.F. Chen: *Mater Charact*, 2022, vol. 185, 111762.
42. H.X. Cao, Q.C. Sun, Q.Q. Pu, L.H. Wang, M.T. Huang, Z.W. Luo, and J.Q. Che: *Vacuum*, 2020, vol. 172, 109063.
43. Z. Zhang, Z.Y. Qiao, X.Y. Wang, Y.B. Guo, and D.G. Wang: *Wear*, 2024, vol. 552–53, 205455.
44. A. Vasconcelos, H. Azevedo, A. Barros, O. Rocha, and M.M. Melo: *Mater. Today Commun.*, 2021, vol. 26, 102099.
45. J.G. Jung, T.Y. Ahn, Y.H. Cho, S.H. Kim, and J.M. Lee: *Acta Mater.*, 2018, vol. 144, pp. 31–40.
46. T. Gao, X.Z. Zhu, H. Qiao, and X.F. Liu: *J. Alloy. Compd.*, 2014, vol. 607, pp. 11–15.
47. R. Haghayeghi, E.J. Zoqui, and G. Timelli: *J. Mater. Process. Tech.*, 2018, vol. 252, pp. 294–303.
48. W.B. Yu, Z.H. Yuan, Z.P. Guo, and S.M. Xiong: *T. Nonferr. Metal. Soc.*, 2017, vol. 27, pp. 2529–38.
49. J.F. Nie, Y.H. Zhao, Y.S. Li, F. Wang, H.B. Yang, K.Q. Hu, G.L. Liu, and X.F. Liu: *J. Alloy. Compd.*, 2019, vol. 777, pp. 8–17.
50. H. Qiao, X.Z. Zhu, T. Gao, Y.Y. Wu, and X.F. Liu: *J. Mater. Sci. Technol.*, 2015, vol. 31, pp. 391–96.
51. K. Zhang, H. Yu, J.Y. Liu, Y.X. Li, J. Liu, and J.L. Zhang: *Mater. Sci. Eng. A*, 2015, vol. 624A, pp. 229–38.
52. H. Wang, P.Y. Yang, W.J. Zhao, S.H. Ma, J.H. Hou, Q.F. He, C.L. Wu, H.A. Chen, Q. Wang, Q. Cheng, B.S. Guo, J.C. Qiao, W.J. Lu, S.J. Zhao, X.D. Xu, C.T. Liu, Y. Liu, C.W. Pao, and Y. Yang: *Nat. Commun.*, 2024, vol. 15, p. 6782.
53. B.Q. Wei, W.Q. Wu, D.Y. Xie, M. Nastasi, and J. Wang: *Acta Mater.*, 2021, vol. 212, 116918.
54. Z.L. Wang, G.Y. Huang, G.R. Zhu, H.C. Hu, C. Li, X.H. Guan, and H.B. Zhu: *Appl. Catal. B Environ.*, 2025, vol. 361B, 124585.

55. L.R. Xiao, Y. Cao, S. Li, H. Zhou, X.L. Ma, L. Mao, X.C. Sha, Q.D. Wang, Y.T. Zhu, and X.D. Han: *Acta Mater*., 2019, vol. 162, pp. 214–25.
56. N.N. Liang and Y.H. Zhao: *J. Alloy. Compd*., 2023, vol. 938, 168528.
57. S.Q. Xiao, S. Hinderberger, K.H. Westmacott, and U. Dahmen: *Philos. Mag. A*, 1996, vol. 73, pp. 1261–78.
58. W.M. Wang, X.F. Bian, J.Y. Qin, and S.I. Syliusarenko: *Metall. Mater. Trans. A*, 2000, vol. 31A, pp. 2163–68.
59. X.B. Yang, K. Fujiwara, R. Gotoh, K. Maeda, J. Nozawa, H. Koizumi, and S. Uda: *Acta Mater*., 2012, vol. 60, pp. 3259–67.
60. J. Wang, Z. Guo, J.L. Song, W.X. Hu, J.C. Li, and S.M. Xiong: *Mater. Des*., 2018, vol. 137, pp. 176–83.
61. N. Ren, C. Panwisawas, J. Li, M.X. Xia, H.B. Dong, and J.G. Li: *Acta Mater*., 2021, vol. 215, 117043.
62. W. Wang, R.G. Guan, Y. Wang, R.D.K. Misra, B.W. Yang, Y.D. Li, and T.J. Chen: *Mater. Sci. Eng. A*, 2019, vol. 751A, pp. 23–24.
63. X.R. Liu, B. Beausir, Y.D. Zhang, W.M. Gan, H. Yuan, F.X. Yu, C. Esling, X. Zhao, and L. Zuo: *J. Alloy. Compd*., 2018, vol. 730, pp. 208–18.
64. S. Beroual, Z. Boumerzoug, and P. Paillard: *Y. Borjon Piron: J. Alloy. Compd*., 2019, vol. 784, pp. 1026–35.
65. S.W. Choia, Y.M. Kima, K.M. Leea, H.S. Cho, S.K. Hong, Y.C. Kim, C.S. Kang, and S. Kumai: *J. Alloy. Compd*., 2014, vol. 617, pp. 654–59.
66. A.M. Samuel, J. Gauthier, and F.H. Samuel: *Metall. Mater. Trans. A*, 1996, vol. 27A, pp. 1785–98.
67. Z.H. Jia, G.W. Zhou, H.Y. Zhou, F. Liu, L.P. Ding, Y.Y. Weng, K.Y. Xiang, and H.D. Zhao: *T. Nonferr. Metal. Soc*., 2024, vol. 34, pp. 737–54.
68. J.W. Xu, W.D. Zeng, X.Y. Zhang, and D.D. Zhou: *J. Alloy. Compd*., 2019, vol. 788, pp. 110–17.
69. L.K. Pillari, K. Lessoway, C. Kuur, A. Lombardi, G. Byczynski, and L. Bichler: *Wear*, 2024, vol. 538–39, 205201.
70. N. Senthilkumar, G. Perumal, S. Sivaguru, and S. Anandhakumar: *Tribol. Int*., 2024, vol. 192, 109232.
71. C.Y. Ouyang, R. Wang, C.J. Zhao, R.Z. Wei, H. Li, R. Deng, Q.F. Bai, and Y.L. Liu: *Tribol. Int*., 2024, vol. 191, 109202.
72. C. Yeh, W. Hsu, B.H. Liu, C.S. Yang, C.Y. Kuan, Y.C. Chang, K.S. Huang, S.S. Jhang, C.Y. Lu, P.K. Liaw, and C.F. Shih: *Nat. Commun*., 2024, vol. 15, p. 4554.
73. Y.G. Liang, S. Lee, H.S. Yu, H.R. Zhang, Y.J. Liang, P.Y. Zavalij, X. Chen, R.D. James, L.A. Bendersky, A.V. Davydov, and X.H. Zhang: I: *Nat. Commun*., 2020, vol. 11, p. 3539.
74. A. Kazimirov, J. Zegenhagen, and M. Cardona: *Science*, 1998, vol. 282, pp. 930–32.
75. T. Uesugi and K. Higashi: *Comput. Mater. Sci*., 2013, vol. 67, pp. 1–10.
76. Y.F. Guo, H.L. Liao, C. Chang, X.C. Yan, Z.Y. Deng, D.D. Dong, Q.K. Chu, Y. Deng, and M. Liu: *Mater. Sci. Eng. A*, 2022, vol. 854A, 143870.
77. A. Vencl, I. Bobić, and Z. Mišković: *Wear*, 2008, vol. 264, pp. 616–23.
78. M. Elmadagli, T. Perry, and A.T. Alpas: *Wear*, 2007, vol. 262, pp. 79–92.
79. Q. Zhang, Y.N. Wu, T.F. Li, C. Qiu, S.Q. Wang, F.J. Fan, H. Teng, C.M. Liu, H. Liu, A.B. Ma, and J.H. Jiang: *Mater. Sci. Eng. A*, 2022, vol. 861A, 144359.
80. A. Eshaghi, H.M. Ghasemi, and J. Rassizadehghani: *Mater. Des*., 2011, vol. 32, pp. 1520–25.
81. F. Alshmri, H.V. Atkinson, S.V. Hainsworth, C. Haidon, and S.D.A. Lawes: *Wear*, 2014, vol. 313, pp. 106–16.
82. R. Taghiabadi, H.M. Ghasemi, and S.G. Shabestari: *Mater. Sci. Eng. A*, 2008, vol. 490A, pp. 162–70.
83. H. Tan, S. Wang, Y. Yu, J. Cheng, S.Y. Zhu, Z.H. Qiao, and J. Yang: *Tribol. Int*., 2018, vol. 122, pp. 228–35.
84. A. Hekmat-Ardakan, X.C. Liu, F. Ajersch, and X.G. Chen: *Wear*, 2010, vol. 269, pp. 684–92.
85. G. Di Egidio, C. Martini, J. Börjesson, E. Ghassemali, L. Ceschini, and A. Morri: *Wear*, 2023, vol. 516–17, 204602.